

## Acoustic Power Divider Based on Compressibility-Near-Zero Propagation

Hussein Esfahlani<sup>1,2,3,4,†</sup>, Matthew S. Byrne<sup>1,2,5,†</sup>, and Andrea Alù<sup>1,2,3,6,\*</sup>

<sup>1</sup>*Electrical Engineering Institute, École Polytechnique Fédérale de Lausanne (EPFL), CH-1015 Lausanne, Switzerland*

<sup>2</sup>*Department of Electrical & Computer Engineering, The University of Texas at Austin, Austin, Texas 78712, USA*

<sup>3</sup>*Photonics Initiative, Advanced Science Research Center, New York, New York 10031, USA*

<sup>4</sup>*Kymeta Corporation, Redmond, Washington 98052, USA*

<sup>5</sup>*Naval Surface Warfare Center Carderock Division, West Bethesda, Maryland 20817, USA*

<sup>6</sup>*Physics Program, Graduate Center, New York, New York 10016, USA*

(Received 1 May 2020; revised 25 June 2020; accepted 13 July 2020; published 20 August 2020)

Materials with properties that can be described by a near-zero index of refraction have received significant attention in the fields of electromagnetics, optics, and acoustics, due to their extraordinary capabilities in wave manipulation. It was recently demonstrated theoretically and experimentally that acoustic waves could manifest near-zero-index propagation based on the effective compressibility of a waveguide channel approaching zero. In turn, this allows tunneling of acoustic waves with nearly infinite wavelength (or equivalently, uniform phase) when the channel cross section is much larger than the feeding lines. Here, we show that these concepts can be leveraged to realize an acoustic power divider and multiplexer offering tunneling of sound to an arbitrary number of output ports, with phase shifts equal to  $0^\circ$  or  $180^\circ$  and robust response to variations in the port position. We present analytical and numerical models describing the properties of this device and study limitations and trade-offs that occur in the presence of losses as the device size is scaled.

DOI: 10.1103/PhysRevApplied.14.024057

### I. INTRODUCTION

Recently, near-zero-index metamaterials have received significant attention due to their extraordinary properties in wave manipulation, which stem from their temporally and spatially decoupled nature [1]. Although the majority of this research has been in the realm of electromagnetics, based on media with near-zero permittivity, near-zero permeability, or double-near-zero materials [2,3], recent attention has also been given to analogous phenomena in the fields of plasmonics [4], photonics [5,6], and acoustics [7]. Several phenomena, such as supercoupling [7], nonreciprocal emission [8], and cloaking [9], have been developed in near-zero-index media both for electromagnetic and acoustic fields. Numerous applications have been also proposed and experimentally validated, such as increasing the directivity of a radiating body [10], realizing a monopolar electromagnetic antenna [11], an acoustic leaky-wave antenna with broadside radiation [12,13], an electromagnetic  $N$ -port series power divider [14–17], and general impedance matching [18].

Among the proposed applications, the  $N$ -port series power divider is of interest in both microwave and

acoustical engineering, because power dividers are used for dividing signals between amplifier chains, for feeding networks in arrays, and for the distribution of signals to multiplexed subsystems[14]. Power dividers, as an essential part of the feeding network, are classified in three different categories, parallel, series, and hybrid (parallel-series), each having their own advantages, disadvantages, and specific applications [19]. For example, the use of antenna arrays with equal amplitude and phase excitation, presenting a main radiation beam at broadside, is popular in communication systems. Similar to electromagnetics, three types of acoustic feeding networks (parallel, series, or hybrid) can be employed. Series power dividers are preferred when we deal with a limited physical space, because parallel-divider-based networks are usually bulky due to the three-port geometry [14]. In a series feed network, meander lines are typically leveraged to ensure that each radiating element is fed with equal-amplitude and equal-phase signals. Hence, there is a cumbersome requirement that the signal is sampled from the meander feed line at locations that are integer multiples of the guided wavelength [15]. Therefore, although series power dividers have many advantages, they also have drawbacks, such as additional design complexity, restrictions imposed upon the placement of elements in the array, and they must be custom tailored according to the number of elements [16].

\*aalu@gc.cuny.edu

†These authors contributed equally to this work.

Near-zero index media provide interesting opportunities in this context, because their largely stretched wavelength ensures phase uniformity over long distances, and hence, another type of series power divider can be envisioned, in which the aforementioned drawbacks can be overcome and significant size reductions compared with meander line series power dividers may be achieved. Here, we explore the design of an acoustic power divider relying on compressibility-near-zero (CNZ) media. To this end, we apply recent theoretical and experimental findings in realizing a CNZ supercoupling medium [7] to design an  $N$ -port acoustic series power divider. We provide analytical and numerical modeling to prove and support these concepts. Then, the proposed  $N$ -port series power divider is shown to support operation with several ports arbitrarily positioned, ensuring equal amplitude and phase power division. The divider may also be configured to divide the signal with a phase flip of  $\pi$  radians, alongside equiphase output ports. Finally, an analysis of practical trade-offs due to losses is presented within a broader discussion on the scalability of the proposed device.

## II. THEORY

In a zero-index material, the governing wave equations are temporally and spatially decoupled [2]. For acoustic phenomena, this property results in a pressure field that is uniform throughout the medium; therefore, if the signal is sampled from such a medium at different points, the output signals are expected to have equal phase. To demonstrate this phenomenon, let us consider the scenario where several input and/or output channels are connected to an intermediate medium with near-zero-index properties, as shown in Fig. 1.

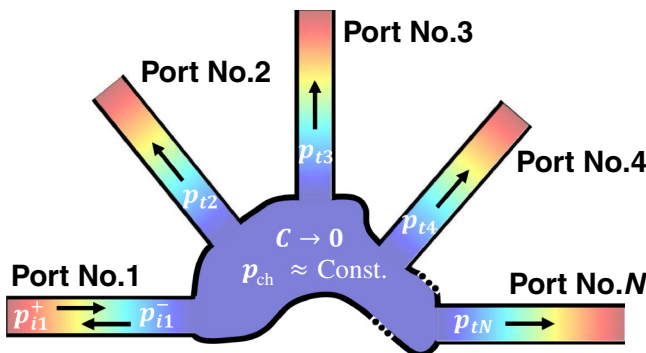


FIG. 1. Arbitrarily shaped acoustic power divider formed by an intermediate channel with near-zero compressibility. Material property of the channel results in a quasistatic acoustic field, having uniform pressure everywhere. When channels meet the matching conditions derived in the text, the input power is fully transmitted and equally split among the outputs.

### A. Equiphase power division

Specifically, we assume that the effective compressibility,  $C_{\text{eff}}$ , is near zero, and thus,  $\lambda = (1/f)\sqrt{(1/C_{\text{eff}}\rho_{\text{eff}})} \rightarrow \infty$ . Channel no. 1, with characteristic acoustic impedance  $Z_1$ , carries the input signal, while the other channels, with characteristic acoustic impedance  $Z_j$ , connect to the output ports.  $Z_j$  is defined as  $Z_j = (\rho_j c_j)/A_j$ , where  $j \in [2, N]$  is the index of each output channel and  $\rho_j$ ,  $c_j$ , and  $A_j$  are the mass density, sound velocity, and cross-section area of channel  $j$ , respectively.

The pressure in the CNZ medium connecting different channels is constant because  $\lambda \rightarrow \infty$ , and hence, the pressure boundary condition becomes

$$p_{i1}^+ + p_{i1}^- = p_{\text{ch}} = p_{t2} = p_{t3} = \dots = p_{tN}, \quad (1)$$

where  $p_{\text{ch}}$  is the uniform pressure in the CNZ medium. Equation (1) implies that

$$1 + R_1 = T_2 = \dots = T_N, \quad (2)$$

where  $R_1$  and  $T_x$   $x \in [2, N]$  are the reflection and transmission pressure coefficients of the input and output channels, respectively. For similarly sized cross sections, the large characteristic impedance of the CNZ medium implies very poor matching and  $R_1 = -1$ . However, if the cross-section area of the CNZ buffer is much larger, as sketched in Fig. 1,  $Z_{\text{ch}}$  can be impedance matched to any of the ports, as experimentally shown in Ref. [7] for acoustic tunneling between two ports. Interestingly, this tunneling is independent of the shape and form of the CNZ buffer, as long as the impedance-matching condition is satisfied by increasing the overall cross-section area.

Hence, if we assume that the CNZ section is impedance matched to port no. 1, we can write, generally, for the volume velocity,  $q$ ,

$$q_{i1}^+ + q_{i1}^- = q_{\text{ch}} = q_{t2} + q_{t3} + \dots + q_{tN}, \quad (3)$$

which can be written in terms of pressure as

$$\frac{p_{i1}^+ - p_{i1}^-}{Z_1} = \frac{p_{t2}}{Z_2} + \frac{p_{t3}}{Z_3} + \dots + \frac{p_{tN}}{Z_N}, \quad (4)$$

and in terms of reflection and transmission coefficients

$$1 - R_1 = Z_1 \left( \frac{T_2}{Z_2} + \frac{T_3}{Z_3} + \dots + \frac{T_N}{Z_N} \right). \quad (5)$$

By substituting Eq. (2) into Eq. (5), the reflection and transmission coefficients of the input and output channels are

derived and expressed, respectively, by

$$R_1 = \frac{1 - Z_1 \sum_{j=2}^N Z_j^{-1}}{1 + Z_1 \sum_{j=2}^N Z_j^{-1}}, \quad (6)$$

$$T_x = 1 + R_1 = \frac{2}{1 + Z_1 \sum_{j=2}^N Z_j^{-1}}, \quad x \in [2, N], \quad (7)$$

where the power transmission and reflection coefficients are defined by  $T_{\Pi x} = (Z_1/Z_x)|T_x|^2$  and  $R_{\Pi 1} = |R_1|^2$ , respectively [20]. For a two-port structure with  $Z_1 = Z_2$ , for instance, no signal is reflected back towards the input, while all of the energy is tunneled through the intermediate CNZ buffer towards the output, independent of its shape or size.

Let us now consider the special case for which the characteristic acoustic impedance of the input and/or output channels are all the same ( $Z_1 = Z_2 = \dots = Z_N$ ), corresponding to transmission lines consisting of the same medium and physical cross section, for instance. This assumption results in the following expressions for the reflection and transmission coefficients for amplitude and power:

$$R_1 = \frac{2}{N} - 1, \quad R_{\Pi 1} = \frac{4}{N^2} - \frac{4}{N} + 1, \quad (8)$$

$$T_x = \frac{2}{N}, \quad T_{\Pi x} = \frac{4}{N^2}, \quad (9)$$

where  $N$  is the total number of ports in the power divider ( $N \geq 2$ ). Equations (8) and (9) reveal that (i) since the CNZ buffer is assumed to be lossless, energy conservation is satisfied with  $R_{\Pi 1} + (N - 1)T_{\Pi x} = 1$ ; (ii) if the number of output channels is increased, the amount of reflected power rises; and (iii) the amount of transmitted power in each channel is inversely proportional to the square of the number of output ports. These findings are consistent with the quasistatic nature of the CNZ buffer, for which what matters to evaluate transmission is the overall area of the output versus input ports normalized to their impedance.

### B. Equiphase zero-reflection power division

As a corollary of the previous findings, we find from Eqs. (6) and (7) that, when the number of output ports is larger than one, the reflected power can be suppressed if

$$Z_1^{-1} = \sum_{j=2}^N Z_j^{-1}. \quad (10)$$

Hence, as far as this Eq. (10) is satisfied, the input power can be ideally split among the output ports with equal phase and without reflection, irrespective of the distribution of the acoustic characteristic impedance of the output ports.

### C. Equiphase and equiamplitude zero-reflection power division

While suppressing reflection in the input channel, the output power can be evenly divided among the ports, if the characteristic impedance of each output port ( $Z_j$ ) is equal. To demonstrate this property, Eq. (10) can be further expanded using the material properties, as well as geometrical dimensions of the channel, as

$$\frac{A_1}{\rho_1 c_1} = \frac{A_2}{\rho_2 c_2} + \frac{A_3}{\rho_3 c_3} + \dots + \frac{A_N}{\rho_N c_N}. \quad (11)$$

If the material inside the input and output channels is the same, or, in other words, the specific acoustic impedances of the channels are equal, Eq. (11) is simplified to

$$A_1 = A_2 + A_3 + \dots + A_N. \quad (12)$$

Finally, to create equiamplitude output,  $A_2 = A_3 = \dots = A_N$ . This relation reveals a matching condition for the CNZ power divider that completely suppresses the reflected power from the input. For this to happen, the sum of the cross-section areas of the output channels should be equal to the cross-section area of the input channel.

## III. REALISTIC IMPLEMENTATION AND SIMULATIONS

Now, we turn to the realistic implementation of a CNZ power divider. We recently showed that it was possible to implement an effective near-zero compressibility by exciting a hard-walled acoustic waveguide with a rectangular cross section at exactly the cutoff frequency of its (2, 0) mode [7]. As mentioned above, to achieve good impedance matching, the ratio of the cross-section areas of the input and/or output waveguides to the intermediate tunneling channel should be made very small, i.e.,

$$A_j \ll A_{ch} \quad \forall j \in [1, N], \quad (13)$$

where  $A_{ch}$  is the cross-section area of the intermediate channel exhibiting CNZ properties and  $N$  is the total number of waveguides connected to the intermediate channel.

Following these principles, a finite-element model is constructed in COMSOL Multiphysics, employing the pressure acoustics module and frequency domain solver. Sound-hard boundary conditions are used to model the walls of the input and/or output waveguides and the intermediate channel, and air is chosen as the filling material. The final layout is shown in the inset of Fig. 2 with dimensions  $a = 0.450$  m,  $b = 0.382$  m, and  $L = 0.79$  m, similar to the experimental setup in Ref. [7].

### A. Lossless case

Figures 2(a) and 2(b) show the power reflection and transmission coefficients for a four-port CNZ power

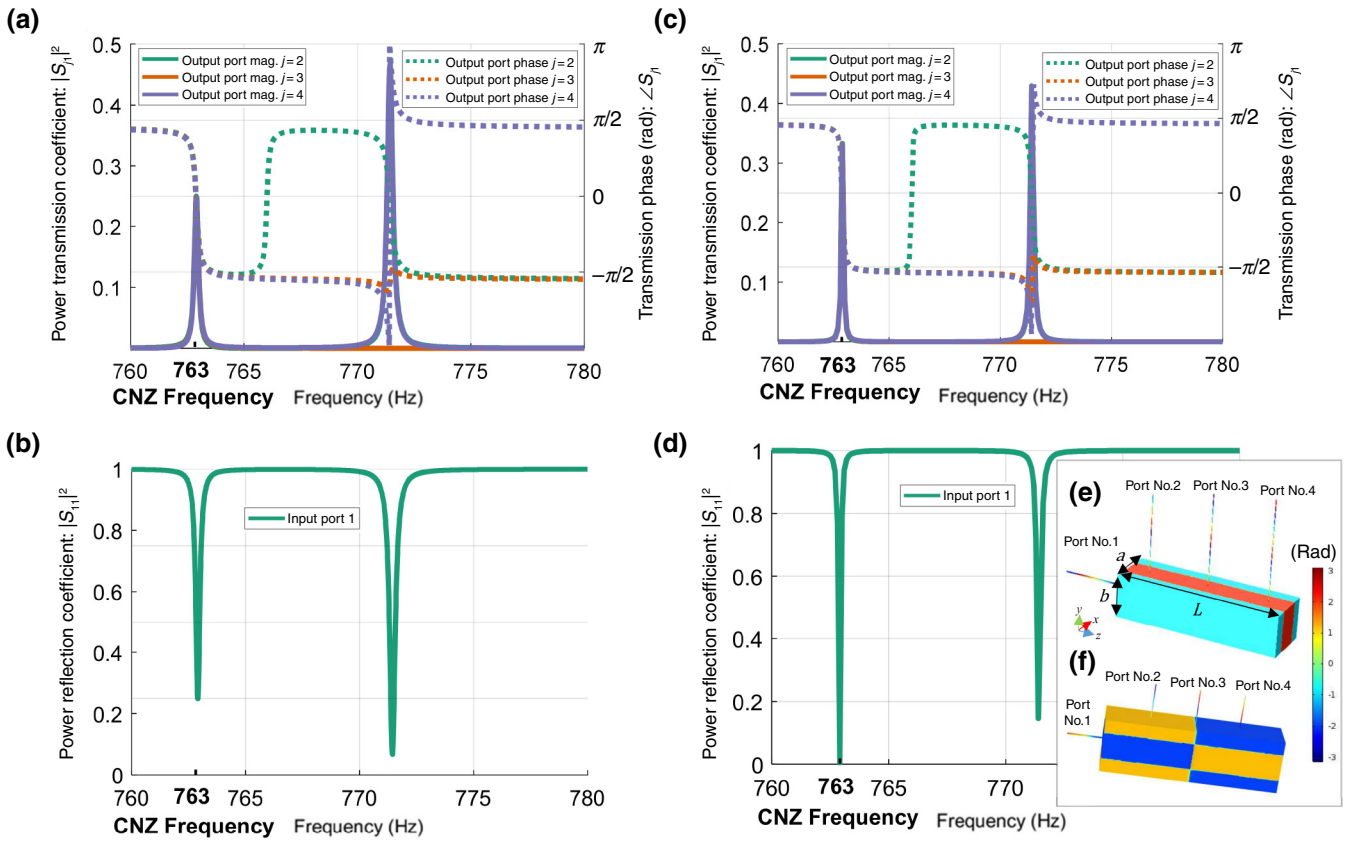


FIG. 2. Geometrical configuration and phase distribution of the uniform-phase equal-amplitude acoustic power divider (bottom-right inset). System is composed of hard-walled cylindrical waveguides for the input (port no. 1) and outputs (port nos. 2–4) connected to an intermediate hard-walled channel with rectangular cross section. Operated at its second cut-off frequency, the intermediate channel performs as an effective CNZ medium and results in uniform-phase output signals. Moreover, equal cross-section areas of the output waveguides results in equal distribution of output power among them. (a) Power transmission coefficient and phase show that the power is divided evenly ( $|S_{j1}| = 0.25$ , where  $j \in [2, 4]$ ) with equal phase among three output ports at the CNZ frequency of 763 Hz. (b) Power reflection coefficient reveals that we observe nonzero reflection at the input port ( $|S_{11}| = 0.25$  at 763 Hz), and therefore, not all of the power is transmitted. (c) Power transmission coefficient and phase of the power divider from (a), but modified, such that the cross-section area of the input waveguide is equal to the sum of the cross-section areas of the output waveguides ( $r_i = 6.3$  mm,  $r_o = 6.3/\sqrt{3}$  mm). Input signal is split evenly ( $|S_{j1}| = 1/3$ ) and with the same phase among the three output ports at the CNZ frequency of 763 Hz. (d) Reflected power at the CNZ frequency is now completely suppressed due to the matching condition, as dictated by Eq. (12). (e) Spatial phase distribution at the CNZ frequency, showing uniformity of the phase of the delivered output signals and the geometrical parameters. (f) Spatial phase distribution for the higher-order mode at 773 Hz. Dimensions of the CNZ channel are  $a = 0.450$  m,  $b = 0.382$  m, and  $L = 1.5$  m. Radii of the input and/or output channels are  $r_i = r_o = 6.3$  mm.

divider. In this configuration, all input and/or output waveguides have the same cross-section areas. The output ports are placed at the top-center of the channel, where the phase of the CNZ resonance is uniform and equal to the input phase. At the CNZ frequency (763 Hz), this geometry results in equal power division with uniform phase to all output ports [Fig. 2(a)]; however, there is some reflection of the incident energy, namely, 25% of the power is reflected back [Fig. 2(b)], in agreement with Eqs. (8) and (9).

To suppress the reflected power and couple all input energy to the output of the system, a second configuration is devised following Eq. (12), as shown in Figs. 2(c)–2(f).

In this case, all dimensions and materials are kept constant with respect to Figs. 2(a) and 2(b), except for the cross-section areas of the output waveguides, which are each smaller by a factor of three. Therefore, the sum of the cross sections of the outputs is equal to the cross section of the input channel, ensuring the matching condition. By examining Fig. 2, we can verify impedance matching at the CNZ frequency, and therefore, full power transmission of the input signal with zero reflection at the input, while the power is split evenly among the three output channels with equal phase.

The CNZ mode profile corresponds to a standing wave in the transverse plane of Fig. 2(e), where the frequency

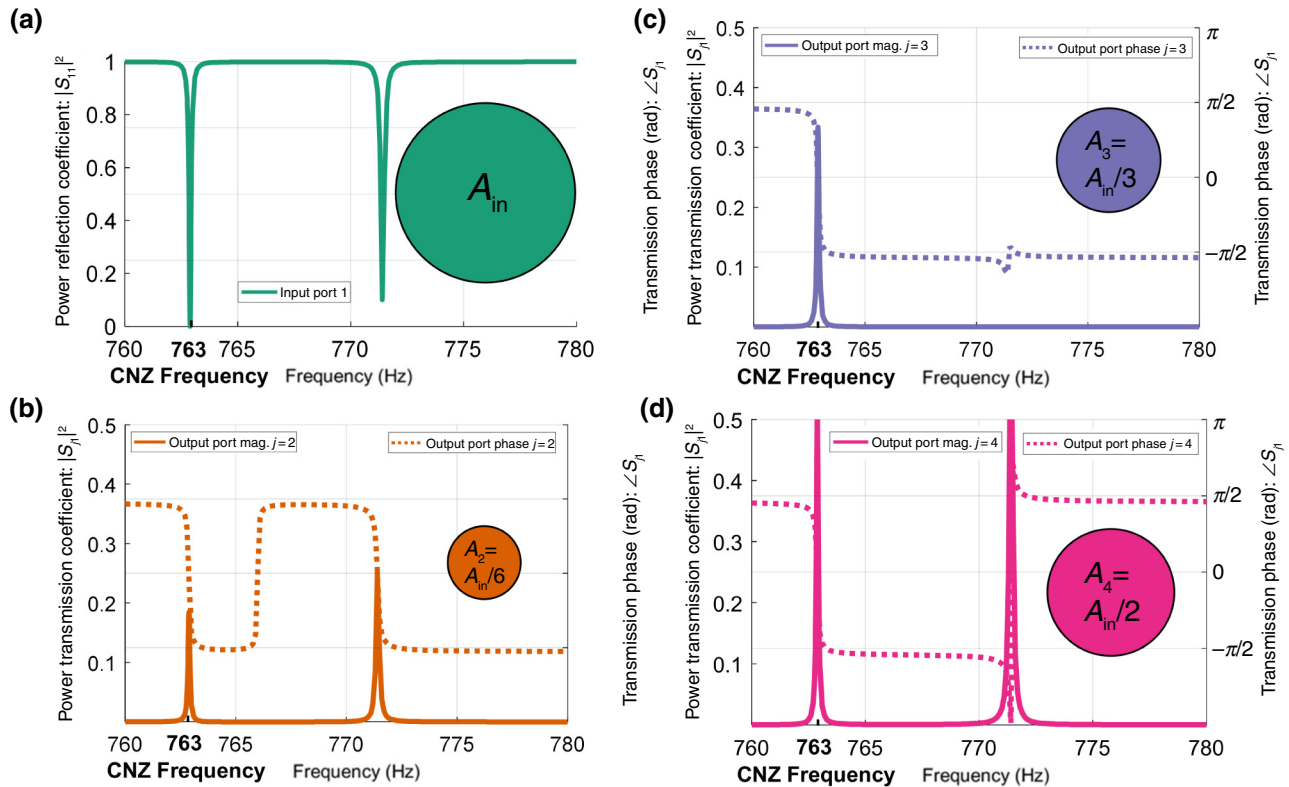


FIG. 3. Matching condition for the input and/or output waveguides in the power divider, Eq. (12), is met with unequal cross-section areas at each output, which allows zero reflection at the input, as well as control over the power supplied to each output port. Geometrical parameters of the power divider are similar to Fig. 2(e), except for the cross-section areas of each input and/or output waveguide, which are indicated by the proportionally scaled insets in all plots ( $r_i = 6.3 \text{ mm}$ ,  $r_{o2} = 6.3/\sqrt{6} \text{ mm}$ ,  $r_{o3} = 6.3/\sqrt{3} \text{ mm}$ ,  $r_{o4} = 6.3/\sqrt{2} \text{ mm}$ ). (a) As the matching condition of Eq. (12) is satisfied, the reflected power remains zero at the CNZ frequency of 763 Hz. (b) Cross-section area of the second output port is  $A_2 = A_{\text{in}}/6$  and the output power is  $|S_{21}|^2 = 1/6$ . (c)  $A_3 = A_{\text{in}}/3$  and  $|S_{31}|^2 = 1/3$ . (d)  $A_4 = A_{\text{in}}/2$  and  $|S_{41}|^2 = 1/2$ .

of the mode depends upon the width of the intermediate channel,  $a$ , and is independent of the length,  $L$ , and the height,  $b$  [given that Eq. (13) is also satisfied]. This property is in contrast with the higher-order tunneling resonances [the second peak in Figs. 2(a) and 2(c)], which are largely affected by variations in the length of the channel, analogous to Fabry-Perot resonances [4]. The phase distribution of this higher-order mode is not uniform along the channel length [see Fig. 2(f)], and therefore, does not provide power equally to all ports.

It should be noted that the matching condition [Eq. (12)] does not require all output ports to have the same cross-section area. Interestingly, when this condition is met with unequal cross sections, the power distribution can be tuned at each of the output ports, as shown in Fig. 3, still ensuring impedance matching at the input port. In this case, the geometrical and material parameters are kept constant with respect to Fig. 2(e), except that the cross-section areas of the outputs are set to  $A_2 = A_{\text{in}}/6$ ,  $A_3 = A_{\text{in}}/3$ , and  $A_4 = A_{\text{in}}/2$ , such that  $A_1 = A_2 + A_3 + A_4$  and Eq. (12) is

satisfied. In turn, this results in an impedance-matched power divider, where no reflection is seen at the input, but where the amount of power distributed to each output is equally proportional to  $A_j/A_1$ , such that  $P_2 = P_{\text{in}}/6$ ,  $P_3 = P_{\text{in}}/3$ , and  $P_4 = P_{\text{in}}/2$ . This tuning of output power can prove useful in several applications. An example may be in making interferometric measurements on a lossy sample, where there are two output waveguides: one is an empty reference waveguide (without material loss) and the second one is filled by some lossy material [21]. By increasing the output power to the waveguide containing the material sample, the system can be designed to compensate for the material loss and then compare the phase of two signals with equal power.

Another unique feature of the proposed configuration is that the phase of the (2, 0) CNZ mode within the channel is flipped by  $180^\circ$  near the boundaries on the sides of the channel (see Fig. 4, top-right inset; also compare with the inset of Fig. 2). In the example demonstrated in Fig. 4, all geometrical and material parameters are the same as

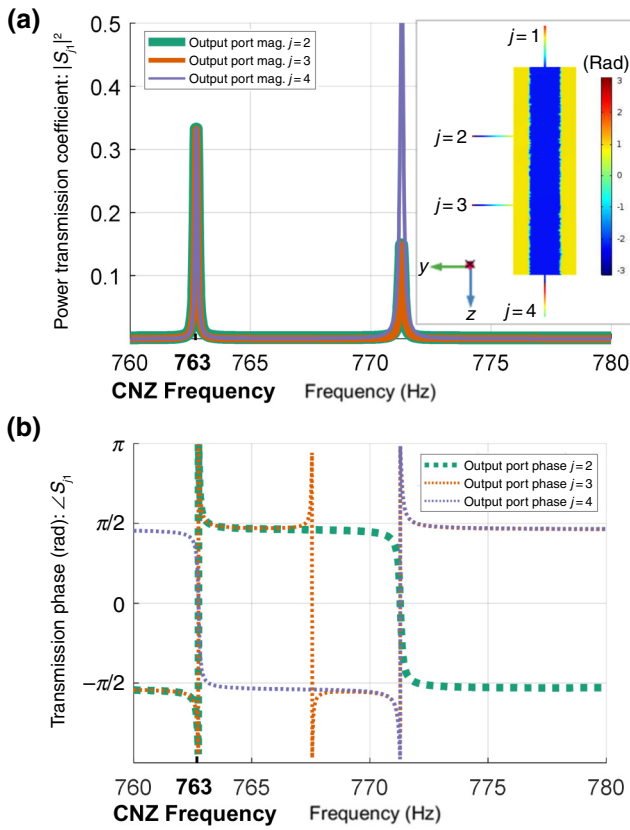


FIG. 4. Geometrical parameters of the power divider are kept identical to Fig. 2(e), except that the output port nos. 2 and 3 are placed along the side of the intermediate channel, while port no. 4 is placed at the end (see spatial phase profile, top-right inset). (a) Power is evenly divided among the three output channels at the CNZ frequency of 763 Hz. (b) At this frequency, the phase is flipped by  $180^\circ$  at the output of both side channels, while the phase is  $0^\circ$  at the interface of port no. 4.

those in Fig. 2(e), except for the location of the output waveguides, which are placed with two outputs along the side and one output along the end face. It can be seen that impedance matching, and thus, full power transmission, is still achieved [Fig. 4(a)], even in this scenario, where the output ports are installed transverse to one another. More importantly, the signal that is coupled to the side channels (nos. 2 and 3) is the phase-inverted ( $180^\circ$  phase flipped) version of the output signal along the end face (channel no. 4). Figure 4 also highlights the capability of inverting the phase of some output channels, while preserving the input phase of the others.

As previously discussed, CNZ-based series power dividers are also expected to have invariant performance with changes in the length and height of the buffer channel. To demonstrate this property, a more general scenario of power divider is shown in Fig. 5, where both the length and height are changed with respect to the previous figures; additionally, the number of output ports is increased

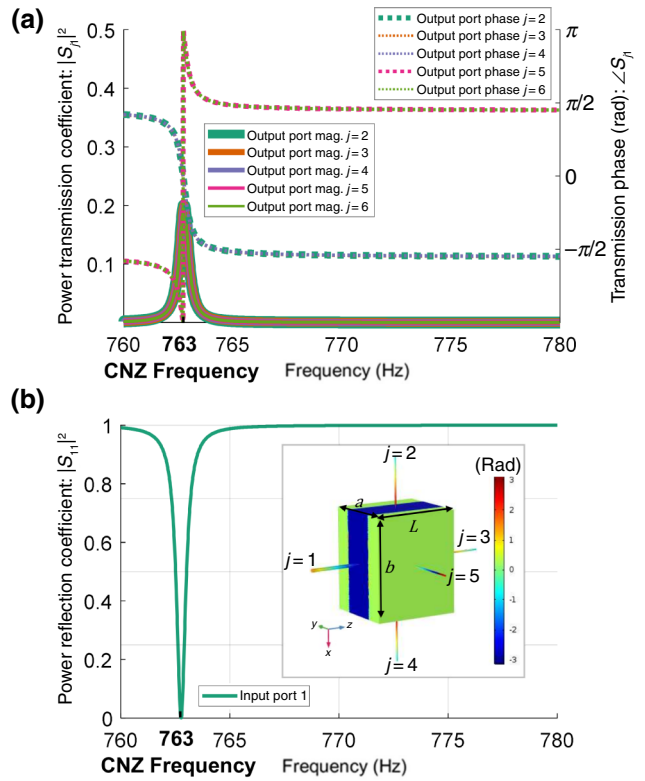


FIG. 5. More general case of the uniform-phase acoustic-power divider, in which the height and length of the channel are varied. This example has a total of five output ports (one on each opposing face of the intermediate channel). Power divider maintains uniform phase for any port placed within  $\lambda/4$  of the center of the channel and the output phase flips by  $180^\circ$  for any output waveguide that is placed elsewhere (see bottom inset). (a) Power is divided evenly among the five output ports at the CNZ frequency of 763 Hz. Phase is zero at the CNZ frequency for port nos. 2–4, and phase is  $180^\circ$  for port nos. 5 and 6. (b) Reflected power remains zero at the CNZ frequency. Dimensions are  $a = 0.450$  m,  $b = 0.6$  m, and  $L = 0.5$  m;  $r_i = 6.3$  mm; and  $r_o = 6.3/\sqrt{5}$  mm.

to five, and the output ports are placed along all faces of the intermediate channel (except for the input face). In this case, the cross-section area of the input port is the same as those in Figs. 2(c) to 4, however, the cross sections of all output ports are now equal to  $A_1/5$ , to satisfy Eq. (12). We see that impedance matching still occurs at the CNZ frequency [Fig. 5(b)], while the phase of the output signal will be either  $0^\circ$  or  $180^\circ$ , depending upon the placement of each port [see Fig. 5(a)].

## B. Modeling radiation losses and their relation to geometric scaling

Finally, we study the scalability of the proposed uniform-phase acoustic power divider and explain how choices of geometrical parameters can have significant

impact, in terms of both the radiation losses and the viscothermal acoustic boundary-layer loss. In this section, we focus the discussion on radiation losses and then consider the impact of viscothermal losses in Sec. III C.

Miniaturization of the power divider is interesting for two reasons: (1) to fit the device into a more compact acoustic system, and (2) to reduce sources of radiation losses compared with those observed experimentally in Ref. [7]. To define miniaturization, we explore downscaling the main geometric parameters of the design in Fig. 2(e), by a constant value, namely,  $a$ ,  $b$ ,  $r_i$ , and  $r_o$ , which represent the width and length of the buffer channel and the radii of the input and output waveguides, respectively. The length  $L$  can also be scaled down in size, but this should not have a major impact on performance due to the length-invariance property of the supercoupling channel. Furthermore, it should be noted that downscaling makes it necessary to increase the operating frequency of the device to maintain operation at the CNZ mode. Finally, we would like to emphasize a fundamental and practical assumption that will be made below: we will *not* assume that the finite wall thickness scales down proportionally to the remainder of the geometry. This is not relevant in the ideal assumption of a hard wall, but it is important when realistic materials are considered. Because of practical limits in cost and weight, a low-audio-frequency CNZ supercoupling channel may require steel walls with thicknesses exceeding 20 mm to keep radiation losses reasonably low. Consequently, by obeying the requirement that  $a = \lambda$ , such a device could weigh in excess of 120 kg. We show that, by considering scaling, a CNZ power divider may be constructed for operation at higher frequencies with much more reasonable choices for size, resulting in a device with lower values for radiation loss, weight, material cost, and geometrical footprint.

We can describe the radiation loss in the CNZ channel due to the finite thickness of a nearly sound-hard wall (e.g., a steel wall with  $h = 1.5$  mm) by characterizing the CNZ channel as a resonant cavity with a total quality factor, sum of a loaded and unloaded quality factor, given by  $(1/Q) = (1/Q_{\text{loaded}}) + (1/Q_{\text{unloaded}})$  [22]. The loaded quality factor represents the case when the input and/or output waveguides (which act as the load) are attached to the buffer, but the channel has perfect hard boundaries, resulting in no radiation. The unloaded quality factor represents the case when the input and/or output ports are blocked (in other words, the load is removed) and the boundaries allow for radiation. The former scenario is already modeled in the numerical results from Figs. 2–5, where, for example, in Fig. 2(c), the channel has  $Q_{\text{loaded}} \equiv (f_r/\Delta f) \approx 6400$ . This value can change slightly, depending upon length, height, and number of output ports; however,  $Q_{\text{loaded}} \approx 6400$  is used as a benchmark in the following example.

Now, we seek to find an expression for  $Q_{\text{unloaded}} \equiv 2\pi(W_{\text{stored}}/W_{\text{rad}})$  (where  $W_{\text{stored}}$  is the stored energy in

the cavity per period and  $W_{\text{rad}}$  is the radiated energy per period). First, we approximate the power lost due to radiation from each transient reflection by using the power transmission coefficient through an acoustic slab with finite thickness  $h$  at normal incidence [23]:

$$T_{\pi c} = \frac{4}{4\cos^2(k_{\text{steel}}h) + \left[ \left( \frac{Z_{\text{steel}}}{Z_{\text{air}}} + \frac{Z_{\text{air}}}{Z_{\text{steel}}} \right)^2 \sin^2(k_{\text{steel}}h) \right]}. \quad (14)$$

The normal incidence assumption is justified because the monomodal (2, 0) mode in the cavity resonates in the direction normal to the boundaries ( $x$  direction, as in the inset of Fig. 2), from which nearly all of the radiation should occur. Hence, a standing wave in the resonator with power  $P_{\text{stored}} = (|\bar{a}|^2/2Z_{\text{air}})$  will lose an amount of power  $T_{\pi c}(|\bar{a}|^2/2Z_{\text{air}})$  at the first transient reflection and it will lose  $T_{\pi c}(1 - T_{\pi c})(|\bar{a}|^2/2Z_{\text{air}})$  at the second transient reflection (where there are two reflections in each period of the resonance of the intermediate channel and  $\bar{a}$  is the wave amplitude in the intermediate channel). If we assume that  $(1 - T_{\pi c}) \approx 1$  [for example, for the intermediate channel of Figs. 2–5,  $T_{\pi c} \approx 2.25 \times 10^{-4}$ , with  $Z_{\text{air}} = 415$  rayl,  $Z_{\text{steel}} = 4.7 \times 10^7$  rayl,  $k_{\text{steel}} = (\omega/c_{\text{steel}})$ , and  $c_{\text{steel}} = 6100$  m/s], then the power radiated upon each reflection is  $T_{\pi c}(|\bar{a}|^2/2Z_{\text{air}})$ , with a total of two reflections per period. This results in a radiated power per cycle  $P_{\text{rad}} = T_{\pi c}(|\bar{a}|^2/Z_{\text{air}})$  and, in terms of energy, we have  $W_{\text{rad}} = (2\pi/\omega)P_{\text{rad}}$ . Next, to find  $W_{\text{stored}}$ , it is assumed that the stored energy per period in the resonator is twice the energy density of a half-period multiplied by the length of the cavity, meaning  $W_{\text{stored}} = 2(P_{\text{stored}}/c_0)L = 2[(|\bar{a}|^2/2Z_{\text{air}})]/c_0L = (|\bar{a}|^2L/Z_{\text{air}}c_0)$ , where  $c_0$  is the speed of sound in the medium. Finally, we find

$$Q_{\text{rad}} \equiv Q_{\text{unloaded}} \equiv 2\pi \frac{W_{\text{stored}}}{W_{\text{rad}}} = \frac{\omega L}{T_{\pi c}c_0} = \frac{2\pi}{T_{\pi c}}, \quad (15)$$

where again,  $T_{\pi c}$  is the power transmission coefficient from Eq. (14) and  $a = \lambda$  for the (2, 0) CNZ mode.

Next, we use coupled-mode theory to derive a first-order approximation for the amount of power radiated from the cavity [24]:

$$\frac{d\bar{a}}{dt} = (i\omega_0 - \gamma)\bar{a} + \kappa s_{\text{inc}}. \quad (16)$$

Here,  $\bar{a}$  is the mode amplitude in the cavity,  $\omega_0$  is the cavity resonance frequency,  $\gamma = \gamma_{\text{loaded}} + \gamma_{\text{unloaded}} = (\omega_0/2Q)$  is the total decay rate,  $\kappa$  is the coupling coefficient, and  $s_{\text{inc}}$  is the input waveform. Assuming that we are operating the cavity at the CNZ frequency,  $\omega = \omega_0$  and  $s_{\text{inc}} = e^{i\omega_0 t}$ . From

this, we find

$$|\bar{a}| = \left| \frac{\kappa}{\gamma} \right|, \quad (17)$$

and, given that  $\kappa^2 = 2\gamma_{\text{loaded}}$  and  $P_{\text{loss}} = 2\gamma_{\text{unloaded}}|\bar{a}|^2$  [24],

$$\begin{aligned} P_{\text{loss}} &= 2\gamma_{\text{unloaded}} \frac{|\kappa|^2}{\gamma^2} = \frac{4\gamma_{\text{unloaded}}\gamma_{\text{loaded}}}{(\gamma_{\text{unloaded}} + \gamma_{\text{loaded}})^2} \\ &= \frac{4Q_{\text{unloaded}}Q_{\text{loaded}}}{(Q_{\text{unloaded}} + Q_{\text{loaded}})^2}, \end{aligned} \quad (18)$$

where  $P_{\text{loss}}$  represents the normalized power loss due to radiation and we used the relations  $\gamma_{\text{unloaded}} = (\omega_0/2Q_{\text{unloaded}})$  and  $\gamma_{\text{loaded}} = (\omega_0/2Q_{\text{loaded}})$ . Equation (18) can now be used to approximate the power radiated from the cavity with an acoustic boundary of finite thickness and finite impedance. For illustrative purposes, we will consider the following two cases:

(1)  $f_0 = 763$  Hz, corresponding to the examples presented in Figs. 2–5, with an intermediate channel of width equal to 45 cm, but now with a steel wall of finite thickness equal to 1.5 mm instead of an ideal hard boundary;

(2)  $f_0 = 10\,000$  Hz, corresponding to a power divider that has all dimensions downscaled proportionally to case (1), resulting in a significantly smaller channel width of 3.4 cm, but with the same steel-wall thickness of 1.5 mm.

From Eq. (14), the first case results in  $T_{\pi c} \approx 2.25 \times 10^{-4}$  and  $Q_{\text{unloaded}} = 2.80 \times 10^4$ . Combining these values with the numerical results of  $Q_{\text{loaded}} \approx 6400$ , we find from Eq. (18) that  $P_{\text{loss}} \approx 0.61$ , estimating very high radiation loss at this size scale. In the second case, the scalability of the lossless Helmholtz equation ensures that the *loaded* quality factor of the smaller power divider is the same as that in case (1). Given the new value of  $k_{\text{steel}}$  at 10 kHz in Eq. (14), we observe that  $T_{\pi c} \approx 1.31 \times 10^{-6}$  and  $Q_{\text{unloaded}} = 4.80 \times 10^6$ , resulting in a much lower  $P_{\text{loss}} \approx 0.01$  from Eq. (18). The significantly lower value for  $T_{\pi c}$  in the second case (with a smaller intermediate channel) is intuitively expected, due to the walls being much thicker with respect to the wavelength, changing from  $(\lambda/l) \approx 300$  in the first case to  $(\lambda/l) \approx 23$  in the second case. These results confirm that downscaling the size of the intermediate channel and, consequently, increasing the operating frequency, while keeping the wall thickness constant, can significantly reduce radiation loss from the CNZ power divider.

### C. Influence of the viscothermal acoustic boundary layer

Despite the theoretical benefits of downscaling the size of the system, one major barrier that exists is acoustic-boundary-layer loss, which results from the viscosity of

the medium in contact with the boundary, as well as the thermal conductivity of the waveguide perimeter. Due to this mechanism, losses within the input and output waveguides are expected to increase as their sizes are decreased [23,25]. Therefore, one potential problem resides in the fact that the boundary-layer loss can become a dominating factor in the power divider, due to the vanishingly small radii of the input and/or output waveguides as the entire device is downscaled and we continue to satisfy Eq. (13).

To mitigate the impact of increased boundary-layer loss due to miniaturization of the power divider, we conduct a parametric study to examine the effect of increasing the surface areas of the input and/or output waveguides relative to the cross-section area of the intermediate channel's input face. It is found that, as the size of the input waveguide is increased, both phase uniformity and impedance matching of the CNZ mode begin to degrade. Figures 6(a) and 6(b) show an example in which the radius of the largest waveguide is increased to  $a/8$  (where  $a$  is the width of the intermediate channel) and the radii of all output waveguides are equal to  $a/8\sqrt{5}$  to satisfy Eq. (12). The increased size of the waveguide radius, with respect to the width of the intermediate channel, results in degradation of impedance matching, an increase of the reflected power, and uneven power division [with respect to the previous configurations of Fig. 2(e) through Fig. 5]. Here, the power reflection coefficient reaches a minimum value of 0.03 and it can be compared with previous configurations, which fully satisfy Eq. (13), and show a minimum reflected power close to zero.

As dictated by Eq. (12), we expect the power to be divided equally among the output ports, with power transmission coefficient of 0.2 for each output channel. However, in this case, the power is distributed a bit unevenly at each port, where the minimum power transmission coefficient is 0.181 at port nos. 2 and 4, and the maximum power transmission coefficient is 0.204 at port nos. 3, 5, and 6. This corresponds to a maximum variation of power transmission of 11.5% with respect to the expected value of 0.2. Finally, the phase of the outputs along the central channel are no longer close to zero, but each have shifted to approximately  $\pi/4$  rad. Therefore, we find a clear trade-off in the performance of the power divider as we explore miniaturization: we can trade uniformity of phase and amount of reflection or transmission for decreased boundary-layer loss at miniaturized dimensions.

The impact of boundary-layer loss at various size scales can also be quantified. By considering the scale invariance of the Helmholtz equation in the waveguides and intermediate channel (without boundary-layer loss), all dimensions of the power divider can be decreased proportionally, while the frequency is increased, such that the size of each dimension with respect to  $\lambda$  remains constant. This theoretically yields a device with identical performance, except for the considerations of viscothermal loss, which

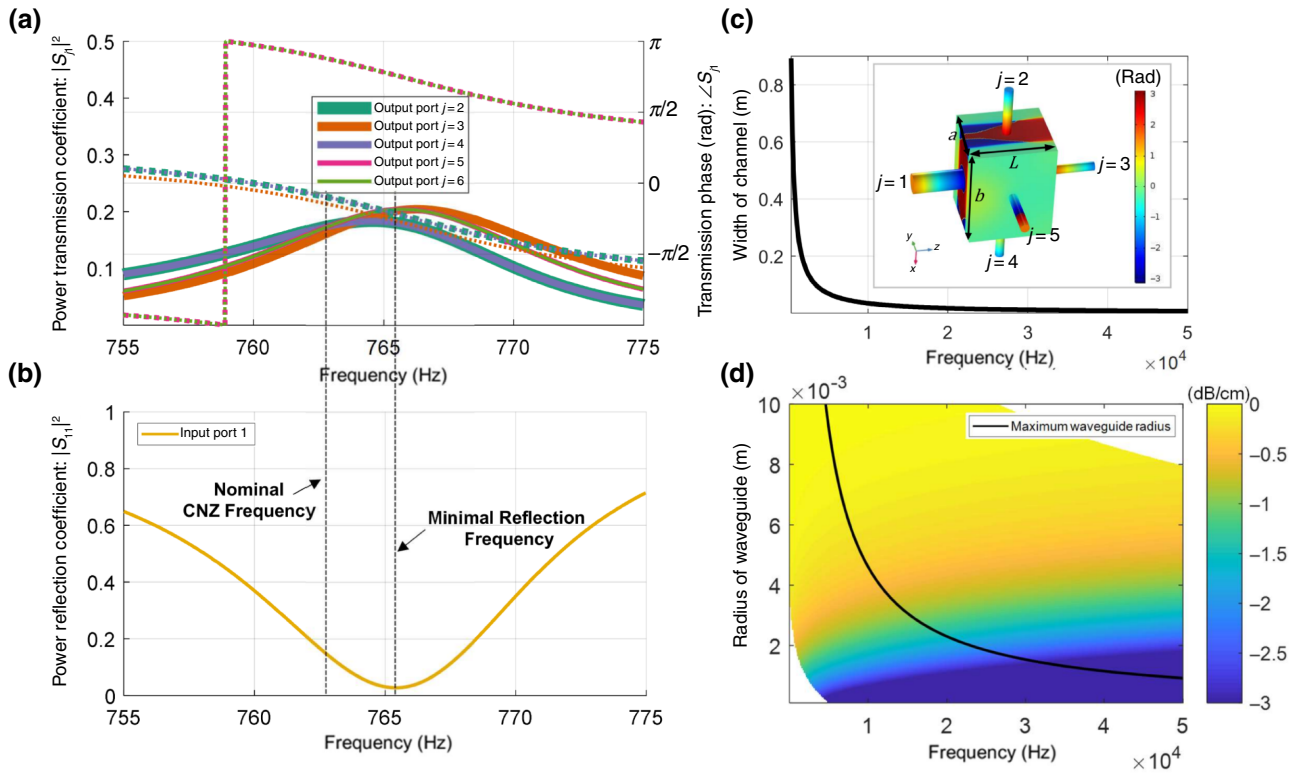


FIG. 6. Scaling limitations for the acoustic power divider. Increasing the size of the input waveguide results in a channel that no longer has uniform phase and the power division becomes uneven. (a) Power transmission coefficients (left axis, solid lines) and phase (right axis, dashed lines) for port nos. 2–6, when the radius of the input waveguide is  $a/8$ , where  $a = 0.450$  m is the width of the intermediate channel. Notably, peak power division no longer occurs at the same frequency for each port, although the output power varies by a maximum of 11.5% in this case. Output transmission phase along the central ports ( $j = 2, 3, 4$ ) increases from zero in the previous case (Fig. 5) to about  $(\pi/4)$  and varies by a maximum of 0.15 rad. (b) Power reflection coefficient for an input waveguide radius of  $a/8$ , which is degraded to 0.03 (compared with the 0 power reflection coefficient of Fig. 5). (c) Variation of the CNZ frequency for a hard-hard channel (where uniform-phase power division can be achieved) as a function of the width of the channel,  $a$ . (d) Viscothermal acoustic boundary-layer loss as a function of frequency and waveguide radius. Black curve represents the limit where input radius reaches  $a/8$ . Below the black curve, all choices of radius and frequency can result in power dividers with approximately uniform phase and equal power splitting. Notably, the units of loss are dB/cm, as we are interested in centimeter-scale devices.

depends upon both the frequency and dimension of each waveguide, and the radiation loss that depends upon the thickness of the waveguide and intermediate channel. Previously, we showed that radiation loss could be controlled independently by setting the thickness of the walls of the intermediate channel. Now, we can predict the boundary-layer loss upon scaling the power divider by considering the smallest input and/or output waveguides in the system, which is the limiting factor contributing most to loss.

We can express the particle velocity in the waveguide as  $u = u_0 e^{-\alpha z} e^{i(\omega t - \beta z)}$ , where for a gas medium

$$\alpha = -\text{Im} \left[ \frac{\omega/c_0}{\sqrt{1 - \frac{2}{r} \left( 1 + \frac{\gamma_{sp}^{-1}}{\sqrt{\text{Pr}}} \right) \sqrt{\frac{v}{j\omega}}}} \right], \quad (19)$$

with  $r$  being the radius of the cylindrical input and/or output waveguide,  $\gamma_{sp}$  is the ratio of specific heats,  $\text{Pr}$  is the Prandtl number, and  $v$  is the kinematic viscosity [23]. By assuming standard atmospheric conditions in air, the implications of Eq. (19) are considered in Fig. 6(d), where we plot the level of insertion loss as a function of waveguide radius and frequency of operation. In particular, we highlight the maximum waveguide radius (black curve) that provides the degradation level in performance reported in Figs. 6(a) and 6(b). This result shows that it is possible to construct an acoustic power divider within an acceptable phase and amplitude variation range by selecting any point in Fig. 6(d) below the black curve. Increasing frequency will result in downscaling the dimension of the coupling channel (where  $a = \lambda$ ), while reducing the radius of the input and/or output waveguide will improve the phase uniformity. Improved phase uniformity comes at the cost of increased boundary-layer loss. Therefore, careful

consideration of the signal requirements for each application should be made before choosing the channel size, the size of the input and/or output waveguides, and the frequency of operation. Furthermore, an alternate route for improving phase uniformity is through increasing the height of the channel ( $b$ ), which has a negligible impact on the operating frequency of the power divider, as shown in Ref. [7]. Finally, it should be noted that the dominant loss mechanism in a given application can be either radiation loss or viscothermal loss, depending on the requirements in terms of material, boundary thickness, frequency, and required length of the connecting channels.

#### IV. CONCLUSIONS

By leveraging recent advances in acoustic supercoupling based on CNZ phenomena [7], we show that an acoustic power divider can be realistically implemented with interesting features, such as the capability of transmitting power with uniform phase to an arbitrary number of output ports, independent of the placement of ports along the central region of the channel. Additionally, it is shown that this power divider can maintain its functionality, independent of changes in length and height of the coupling channel, given that there is a large difference between the cross-section areas of the input and/or output waveguides and the cross-section area of the coupling channel. Furthermore, it is possible to control the amplitude and phase (in increments of  $\pi$  radians) delivered to each output port, without compromising impedance matching. This approach also overcomes limitations of traditional meander-line-based series power dividers, which require the output ports to be constrained to specific locations along the length of the component. We also evaluate the trade-offs between viscothermal loss, radiation loss, phase uniformity, and power splitting in realistic designs, offering a practical avenue towards compact and low-loss CNZ supercoupling power dividers. Our work opens up possibilities for centimeter-scale acoustic supercoupling devices with a variety of potential applications. For example, when used in a pulse-echo measurement system (such as nondestructive evaluation, acoustic imaging, or sonar), this device can be used as a power divider with near-zero-phase filter properties to remove noise or clutter from the received signal, without the need for an additional band-pass filter in the receive chain. Furthermore, the capability of adjusting the output power levels (as shown in Fig. 3) can be leveraged in the design of loss-compensating acoustic interferometers. Finally, the power divider can be used for multiplexing acoustic signals with opposite phases and differing weights.

#### ACKNOWLEDGMENTS

This work is supported by the DoD SMART Scholarship, the Swiss National Science Foundation's (SNSF)

Doctoral Mobility Fellowship Award under Decision No. P1ELP2\_165148, and the National Science Foundation EFRI program. We acknowledge useful discussions with Prof. Dimitrios Sounas.

- 
- [1] N. Engheta, Pursuing near-zero response, *Science* **340**, 286 (2013).
  - [2] I. Liberal and N. Engheta, Near-zero refractive index photonics, *Nat. Photonics* **11**, 149 (2017).
  - [3] M. Silveirinha and N. Engheta, Design of matched zero-index metamaterials using nonmagnetic inclusions in epsilon-near-zero media, *Phys. Rev. B* **75**, 075119 (2007).
  - [4] A. Alù and N. Engheta, Light squeezing through arbitrarily shaped plasmonic channels and sharp bends, *Phys. Rev. B* **78**, 035440 (2008).
  - [5] X. Huang, Y. Lai, Z. H. Hang, H. Zheng, and C. T. Chan, Dirac cones induced by accidental degeneracy in photonic crystals and zero-refractive-index materials, *Nat. Mater.* **10**, 582 (2011).
  - [6] I. Liberal, A. M. Mahmoud, Y. Li, B. Edwards, and N. Engheta, Photonic doping of epsilon-near-zero media, *Science* **355**, 1058 (2017).
  - [7] H. Esfahlani, M. S. Byrne, M. McDermott, and A. Alù, Acoustic supercoupling in a zero-compressibility waveguide, *Research* **2019**, 2457870 (2019).
  - [8] A. R. Davoyan and N. Engheta, Nonreciprocal emission in magnetized epsilon-near-zero metamaterials, *ACS Photonics* **6**, 581 (2019).
  - [9] H. F. Ma, J. H. Shi, Q. Cheng, and T. J. Cui, Experimental verification of supercoupling and cloaking using mu-near-zero materials based on a waveguide, *Appl. Phys. Lett.* **103**, 021908 (2013).
  - [10] S. Enoch, G. Tayeb, P. Sabouroux, N. Guerin, and P. Vincent, A Metamaterial for Directive Emission, *Phys. Rev. Lett.* **89**, 213902 (2002).
  - [11] A. Lai, K. M. Leong, and T. Itoh, Infinite wavelength resonant antennas with monopolar radiation pattern based on periodic structures, *IEEE Trans. Antennas Propag.* **55**, 868 (2007).
  - [12] H. Esfahlani, S. Karkar, H. Lissek, and J. R. Mosig, Acoustic dispersive prism, *Sci. Rep.* **6**, 18911 (2016).
  - [13] H. Esfahlani, S. Karkar, H. Lissek, and J. R. Mosig, Exploiting the leaky-wave properties of transmission-line metamaterials for single-microphone direction finding, *J. Acoust. Soc. Am.* **139**, 3259 (2016).
  - [14] A. Lai, K. M. Leong, and T. Itoh, in *IEEE MTT-S Int. Microw. Symp. Dig.* (2005), pp. 1001.
  - [15] M. A. Antoniades and G. V. Eleftheriades, A broadband series power divider using zero-degree metamaterial phase-shifting lines, *IEEE Microw. Compon. Lett.* **15**, 808 (2005).
  - [16] A. Lai, K. M. Leong, and T. Itoh, in *2005 European Microwave Conference* (2005), pp. 4.
  - [17] H. V. Nguyen and C. Caloz, Tunable arbitrary N-port CRLH infinite-wavelength series power divider, *Electron. Lett.* **43**, 1292 (2007).

- [18] Z. Zhou, Y. Li, E. Nahvi, H. Li, Y. He, I. Liberal, and N. Engheta, General Impedance Matching via Doped Epsilon-Near-Zero Media, *Phys. Rev. Appl.* **13**, 034005 (2020).
- [19] W. L. Stutzman and G. A. Thiele, *Antenna Theory and Design* (Wiley, New York, NY, 1998).
- [20] L. E. Kinsler, A. R. Frey, A. B. Coppens, and J. V. Sanders, *Fundamentals of Acoustics* (John Wiley & Sons, Hoboken, NJ, 1999).
- [21] E. I. Alekseev, E. N. Bazarov, V. P. Gubin, A. I. Sazonov, M. I. Starostin, and A. I. Oussov, Recirculating fibre ring interferometer with compensation for losses in the cavity, *Quantum Electron.* **31**, 1113 (2001).
- [22] D. E. Pozar, *Microwave Engineering* (John Wiley & Sons, Hoboken, NJ, 2009).
- [23] D. T. Blackstock, *Fundamentals of Physical Acoustics* (John Wiley & Sons, Hoboken, NJ, 2001).
- [24] H. Haus, *Waves and Fields in Optoelectronics* (Prentice-Hall, Englewood Cliffs, NJ, 1984).
- [25] T. W. Van Doren, PhD., Dissertation for the University of Texas at Austin, 1993.